SAND2019-14767R

Drag Coefficient Analysis of Arbitrary Fragment Geometry with Emphasis on Meshing Sensitivity Studies

Shivam Barwey

Acknowledgements:
Peter Yeh, Steve Attaway, John Korbin

Sandia National Laboratories

This report characterizes Mach number effects in the hypersonic range from Mach 3 to Mach 7 for an arbitrary, computationally generated fragment. Force and moment coefficients in the x, y, z direction were successfully obtained and resulting trends were compared with theoretical expectations. Three orientations were tested in the form of unit vectors: [1,0,0], [0,1,0], and [0,0,1]; these represent the *i, j, k* principle axes. The final results ultimately showcased a trend very similar to that shown in previous literature – drag coefficients for a given orientation decreased with increasing Mach number by a very small amount in the hypersonic range. It was therefore concluded that the aerodynamic quantities used to obtain the fragment trajectory at low hypersonic Mach numbers (such as Mach 3) can be used to characterize the aerodynamic qualities at higher hypersonic Mach numbers (Mach 5, 7) with a reasonably small margin. A sensitivity study was also conducted which ultimately defined drag effects as a result of changing grid spacing and normal extrusion parameters for the unstructured tetrahedral mesh used in the simulation. Further work can be done in the form of experimental validation, specifically with regards to wind tunnels and ballistic range testing. Error can be reduced by testing more mesh variabilities and capturing a larger amount of fragment orientations. The results for force and moment characteristics dependent on meshing parameters and high Mach numbers are satisfactory and consistent with expected trends.

I. Introduction and Theoretical Background

This study focuses on the aerodynamic quantities of interest, namely drag, of metal fragments as a result of charge geometry and explosive expansions. The analysis below includes detailed characterization of simulation and meshing parameters, force coefficients, and experimental proposals for future computational validation of results.

Due to the inherent arbitrary nature of fragment behavior and geometry, it is often difficult to determine the force behavior and trajectory of the object – however, fundamental aerodynamics at hypersonic velocities can still be applied. The primary forces acting on the fragments which create drag are face drag (dynamic pressure) and base drag (turbulent wake). Base drag and face drag magnitudes are functions of projected fragment face area at a particular instance in time; therefore, it is important to obtain drag quantities as a function of the rotation angles of the fragment about the centroid, as the frontal area of the fragment changes dramatically as it rotates through the air (this will be taken into account in the results below). Fragment drag is also directly related to air density, flight velocity vector, and the drag coefficient as expressed below:

$$F = \frac{C_D A_f \rho_a V_f^2}{2}$$

Where F is the force, C_D is total drag coefficient, A_f is frontal area at the time instance, ρ_a is air density, and V_f is velocity. The total drag coefficient, which is what the simulation below captures, is simply the sum of both face and base drag components. For better understanding of behaviors at a varying range of Mach numbers, typical total drag coefficient (addressed henceforth as drag coefficient) can be calculated for a cube. This results essentially indicate that total drag coefficient for a cube tumbling face-on increases rapidly in the transonic region (Mach

0.8 – 1.1) with a peak at about Mach 1. Drag coefficient values appear to stagnate in the hypersonic regime – quantities decrease by a very small amount as Mach number increases after about Mach 3. These drag coefficient trends are important in fragment flight studies as they allow for a reasonable drag coefficient margins to be met without running simulations at high hypersonic Mach numbers. This is further described and calculated in the results below.

II. Simulation Setup and Meshing Procedure

The fragment simulations were run in an aerodynamic 6DoF simulator with specified infinity flow conditions and SST turbulence models using the RANS equations. Initially, the fragment was placed in a numeric wind tunnel to obtain force coefficients at specified parameters. Then, the resulting coefficients and rotation angles were placed in a 6DoF solver to obtain flight trajectory quantities such as position, velocity, and accelerations at each time-step. A specific heat ratio of *1.4* was used in accordance with air properties, and Prandtl number was set to *0.72* on the same principle. Pressure at flow state infinity was assumed to be atmospheric at *101325 Pa*; temperature was set to *298 K*; turbulence intensity and viscosity ratio were defined to be *0.01* and *0.1* respectively.

With regards to temporal solution parameters, *4000* incremental steps were set for the simulation. Amount of time per step was dependent on the spatial order of the time step itself – for this case, the first 400 time steps were simulated on the first special order, and the remainder steps were computed on the second special order regime.
For the drag coefficient calculations in this experiment, three different Mach numbers were initially tested – Mach 3, 5, and 7. These numbers were chosen to satisfy a reasonable hypersonic range characteristic of the true flight speeds experienced by the fragment upon detonation. Force quantities were also found as a function of fragment position – in this study, only three orientations were tested for the sake of simplicity and brevity on the basis of the {*i, j, k*} unit vectors. That is, the positions of *[1,0,0]*, *[0,1,0]*, and *[0,0,1]* were tested at all specified Mach numbers.

In order to achieve varying orientations of the fragment without changing the mesh entirely, a spherical far-field boundary was used with the fragment surface at the center. This allowed for a simple change in inlet flow direction without changing the mesh itself to represent fragment flight orientation. **Figure 1** below shows an example of a fragment mesh used in the simulation process.

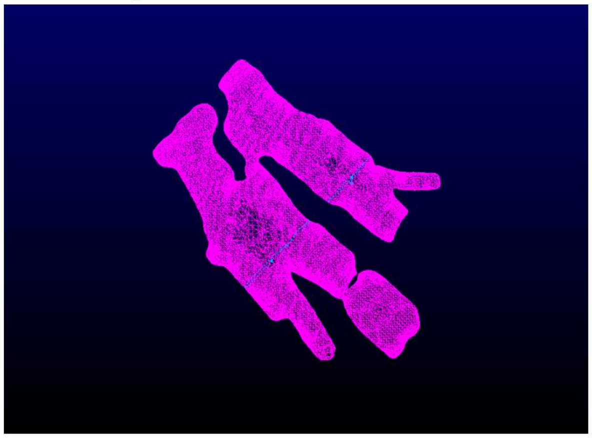

Figure 1. Fragment mesh example.

III. Results and Discussion

a) Mach Number Dependence on Fragment Drag Coefficients

A main objective of the simulations was to characterize a relationship between force coefficients and moment coefficients with respect to supersonic Mach number variation. The similarities and differences with respect to theoretical expectations and trends was also a

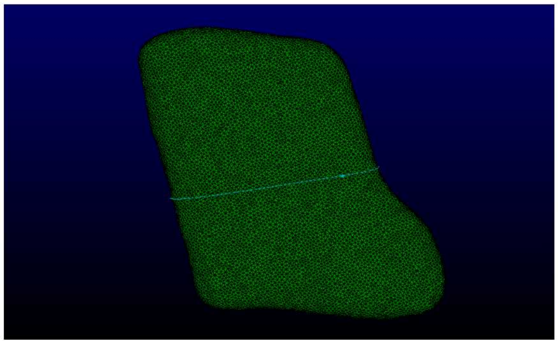

Figure 2. Fragment geometry used in simulations.

major goal. For the following results, the fragment used was the result of a CTH simulation which outputted several STL files of fragment geometries – after various smoothing procedures, the final fragment was able to be meshed successfully with proper refinement around areas of interest. The characteristic length of the fragment used was *0.028 m* tip-to-tip; **Figure 2** displays the fragment geometry in question.

Using the setup described in *Section II*, graphical summaries of the drag coefficients are shown below. **Figure 3** displays coefficient plots for the [1,0,0] orientation.

The force coefficient in the x-direction displays a clear trend of higher coefficient values for lower Mach numbers, which is consistent with supersonic aerodynamic theory. The curve, which represents coefficient versus time-step, shifts downward as Mach number increases, signifying a decrease in immediate downstream drag with higher Mach numbers in flight. Similar trends can be observed for the moment coefficient in the x-direction at a reasonable small magnitude (which is to be expected). Because the fragment is assumed to be rotating at a very small rate compared to its translational speed, this aerodynamic problem can be treated as quasi-steady – this assumption is consistent with what the graphs show, as the magnitude of moment coefficients are considerable smaller than force counterparts. When observing the force coefficient in the y-direction and z-direction for the [1,0,0] fragment orientation, the coefficient curve trends are reversed from those of the x-direction – the curves decrease with decreasing Mach number. The same is true for the corresponding moment curves in the y- and z-direction. This implies that, as Mach number increases, force components that are not of the same component as the incoming flow direction actually increase as Mach number increases in the hypersonic regime. These trends are also observed for [0,1,0] and [0,0,1] flow directions for the same fragment. Furthermore, the described trends are consistent with theoretical expectations of drag forces in the hypersonic regime, which can further validate this simulation.

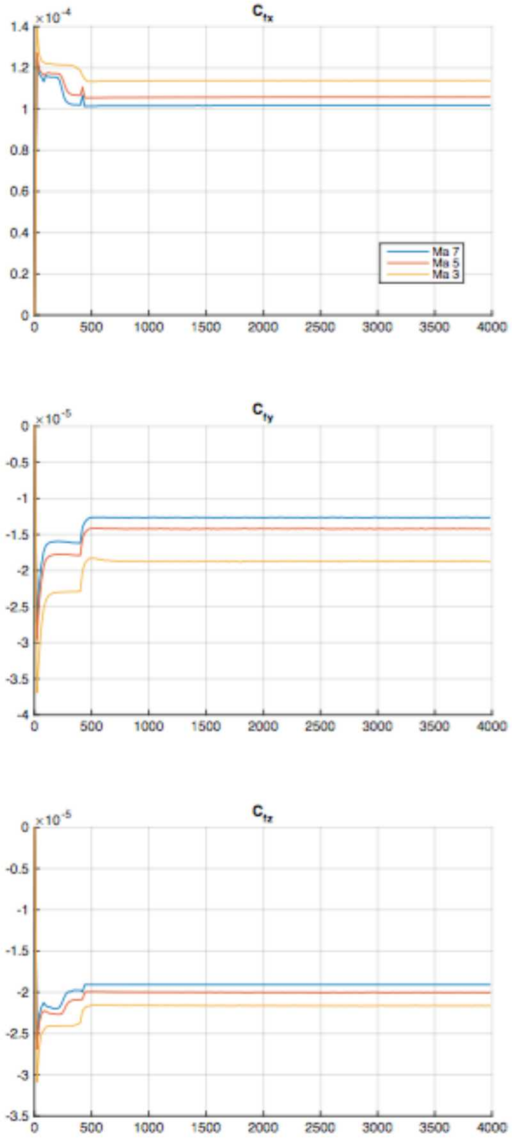

Figure 3. Force coefficient values as a function of iterations for [1,0,0] orientation.

To better visualize Mach number effects on force/moment coefficients, values were averaged over the last 200 iterations (within steady state conditions) and plotted versus each respective Mach number for a given orientation. A summary of the plotted values in **Figure 4** can be seen in **Table 1** in *Appendix Section (e)*, which denotes maximum relative errors.

Each curve on a figure represents one of three tested orientations, and each figure represents a particular force or moment coefficient component. The figure shows that although drag coefficient values drop with increasing Mach number, the amount by which these values drop is relatively small. When compared to Cooper's theoretical expectations as described in *Section I*, the simulation results are ultimately deemed consistent and satisfactory with what is expected with regard to trends. The same can be said for moment coefficients; Mach number changes do affect coefficient values, but not by a substantial amount so as to change simulation parameters to account for Mach number variance in the hypersonic regime. It is therefore more efficient to run simulations at a lower hypersonic Mach number, such as Mach 3, using a reasonable error margin than it is to run a simulation at a higher hypersonic Mach number, such as Mach 7, which runs the risk of flow instability and divergence in the simulation algorithms.

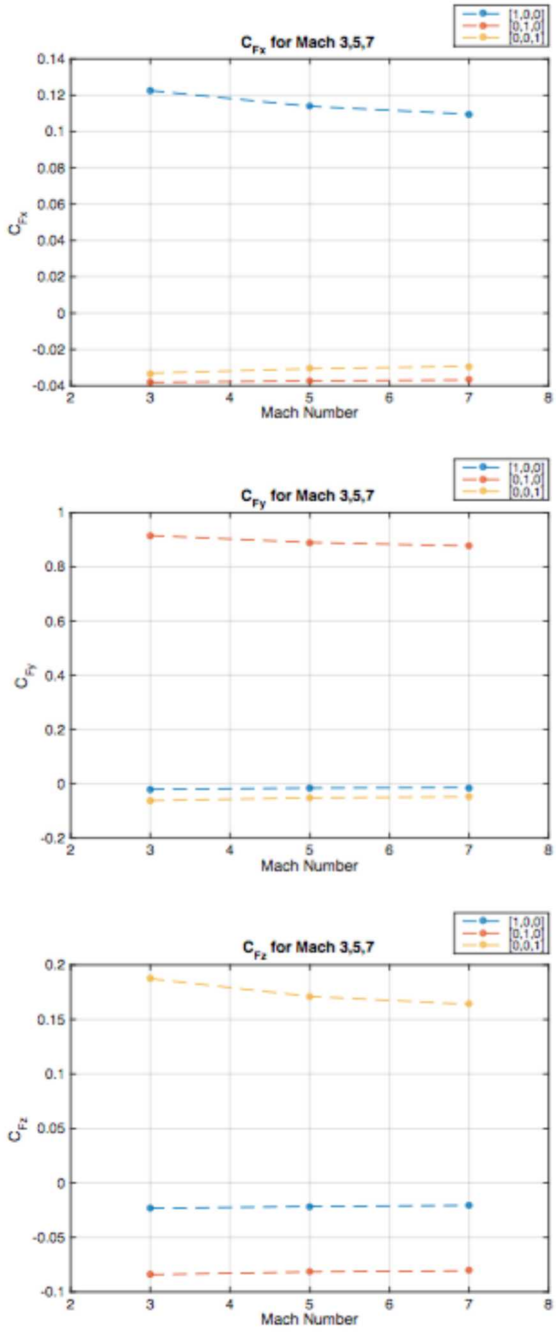

Figure 4. Force coefficient values as a function of Mach number for all tested orientations.

b) Mesh Sensitivity Study on Drag Coefficient Convergence

The standard mesh which includes a non-extruded fragment surface at the center of a spherical far-field boundary was modified with varying sensitivities to conduct a convergence test in order to see the resulting effects on drag coefficients. The unstructured tet-mesh refinement in the domain was modified independently to monitor potential drag effects, as was the mesh refinement on the fragment surface, the surface extrusion steps (if an extrusion was present), and the extrusion growth rate. Five different mesh cases were tested and are summarized below.

<u>Case 1:</u> Default case
$\Delta s_{frag} = 0.0005$
$\Delta s_{farfield} = 0.004$

<u>Case 2:</u> Added a normal extrusion on fragment surface equal to one-fifth of the interior mesh spacing (consistent with previous models).
$\Delta s_{extr} = 0.0001$
$Growth\ rate = 1$
$Ste□s = 20$
$Relaxation\ and\ smoothing\ o□$

<u>Case 3:</u> Modified far-field grid spacing.
$\Delta s_{farfield,ne□} = 0.001$
$\Delta s_{farfield,old} = 0.004$

<u>Case 4:</u> Fragment mesh resolution increased (no extrusion). Ratio of fragment resolution to far-

field resolution remained the same; only decrease in spacing.

$\Delta s_{frag,new} = 0.0003$
$\Delta s_{sphere,new} = 0.0024$

Case 5: Fragment mesh resolution increased with extrusion (same extrusion parameters as Case 2).

$\Delta s_{frag} = 0.0003$
$\Delta s_{farfield} = 0.0024$
$\Delta s_{extrusion} = 0.00006$

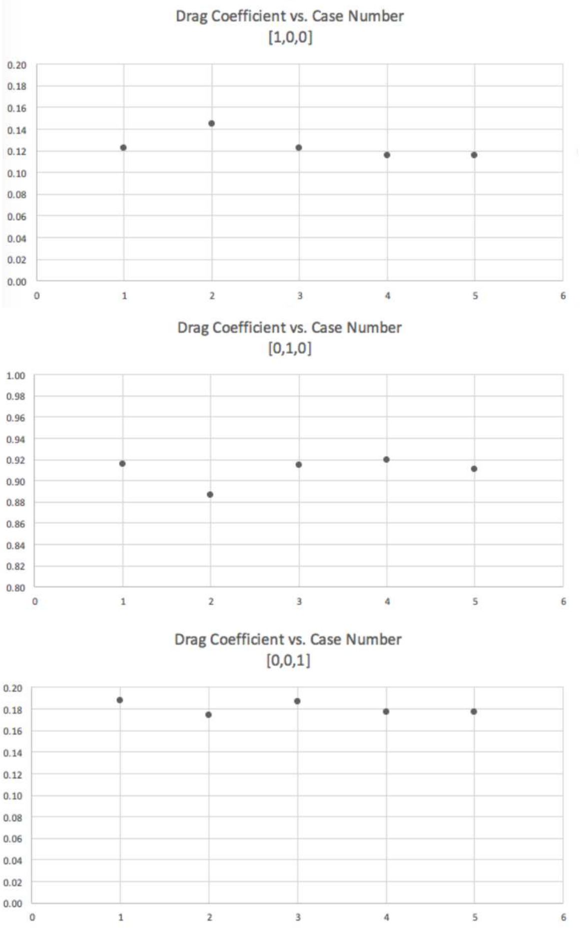

Figure 5. Drag coefficient values as a function of Case number for all tested orientations.

All five cases are summarized in **Tables 2 – 4** in *Appendix section (e)* and **Figure 5** above by order of fragment orientation in the principle axes. The same fragment was run at Mach 3 for all cases. For the [1,0,0] orientation, drag coefficient values (force coefficient in the x-direction) appear to have relatively higher variance than the other values. Case 2 in particular deviates largely from the others, and provides a maximum relative error for this data as *0.198*. Errors on the other coefficients in the [1,0,0] orientation remain below *5%* in all cases and are on track for convergence. The respective figure shows drag coefficient stability with the exception of the Case 2 outlier. For the [0,1,0] orientation, drag coefficient stabilized at about *0.91*. This magnitude is much higher than the [1,0,0] counterpart due to the higher frontal area magnitude. Case 2 for this set of data again deviates from the other cases, but not by a significant amount – the maximum relative error for drag coefficient quantities in the [0,1,0] orientation is a very low *0.04*. For the [0,0,1] orientation, drag coefficient resembles that of the [1,0,0] data – the value stabilized around *0.17* with a maximum relative error of *0.07*. Summary data tables can be found in the *Appendix section*.

IV. Conclusion and Future Work

This study successfully attributed drag coefficient quantities to an arbitrary fragment geometry while characterizing Mach number dependence in the hypersonic range. Furthermore, Mesh sensitivity studies were used to determine the variations in drag coefficient caused by adjusting the grid spacing and normal extrusion properties used on the mesh configuration. To reduce simulation and result error in this study, it is recommended to use a higher amount of meshing cases and test different fragment orientations (only the three principle unit vectors were tested in this experiment). The number of simulation time steps calculated on the second spatial order could also be modified and tweaked to obtain more accurate results. Future work includes completely modelling the three-dimensional flight trajectory based on 6DoF simulations using these coefficient inputs to develop a better understanding of fragment behavior at high speeds and temperature.

Further progress can be made in the form of experimental validation (along with variations in simulation validation). For example, fragment flight and trajectory experiments can be conducted in multisonic/hypersonic wind tunnels or ballistic ranges to validate these experimental results. Three wind tunnel experiments are explained in detail with schematics in the *Appendix section* below – Schlieren imaging, particle image velocimetry techniques, and the application of temperature and pressure sensitive paint on the fragment geometry.

V. References

Yeh, Peter D. *Simulations of Supersonic Fragment Trajectories*, Sandia National Laboratories, Albuquerque, NM. 2016.

Cooper, Paul W. *Explosives Engineering.* Wiley-VCH, Inc. 1996.

Anderson, John D. *Fundamentals of Aerodynamics, 5th Edition.* McGraw-Hill Education. February 12, 2010.

VI. Appendix

The schematics for the following experimental techniques are found in *subsection (d)*. All data tables are found in *subsection (e)*.

a) Schlieren Imaging

A Schlieren imaging setup may be used in this experiment to properly assess density gradient fluctuations and shock-expansion effects on the fragment. Light-ray path along with entire experimental arrangement is shown below. The image (which can be obtained through a color CCD camera) can be displayed using general imaging software such as XCAP. It should be noted that the camera may produce distorted figures; if this is the case, the resulting images' aspect ratios must be corrected to properly represent real conditions. A solution to this issue is to place a transparent grid overlay with known dimensions on the test section window (images can then be corrected using simple photo-editing software).

Schlieren imaging is an interferometric technique which, simply put, relies on the changes in index of refraction of EM propagations through a given medium. For our purposes, index of refraction reacts to changes in both densities of the medium and temperature of the medium (assuming the medium is held constant).

The Gladstone-Dale relation relates refraction index to density:

$$n = \kappa\rho + 1$$

By this relation, we can conclude that light rays turn towards regions of higher density. Because Schlieren imaging is sensitive to the first derivative of density (as opposed to shadowgraph imaging, which is sensitive to the second derivative), higher quality images with respect to shockwaves and expansion fans can be obtained (refer to governing equations for Schlieren and shadowgraph).

Most Schlieren setups involve a white point source light with an iris and color filter to make the incoming light waves uniform to better visualize density gradients in the test section.

A Schlieren setup is very similar to that of a shadowgraph – the only difference is that there is a "spatial filter" (most commonly a Heaviside filter, such as a knife-edge) placed at the second focal point right before the incoming rays hit the camera. A vertical knife-edge orientation will result in horizontal density gradient visualizations; a horizontal knife-edge orientation will result in vertical density gradient visualizations.

b) TSP

A schematic of an example experimental apparatus is shown below. An ultraviolet LED light source is used to excite the TSP molecules on the fragment's surface. Ultraviolet light is much higher in frequency than standard white light – this is needed in TSP experiments because the incident light source must have photons with high enough energy to excite the TSP molecules in order to visualize spectroscopic emission. In other words, to properly image fluorescence which is associated with short-lived de-excitation, UV light is necessary due to its high incident photonic energy. The fluorescent light, as indicated in the figure, is then captured by a CCD camera (ex. Apogee). Fluorescent light properties are dependent on the proportions of quenching/photon emissions, which are related to temperatures and pressures on the model surface. Before the fluorescent light is captured by the camera, it propagates through a yellow glass filter. The purpose of this filter is to narrow the wavelength range for image capture and visualization – "long pass" means that only light of long wavelengths will be imaged by the camera. By narrowing the wavelength range imaged by the camera, quenching and intensity effects can be properly analyzed due to changes in surface pressures and temperatures on the shuttle (along with producing clearer images). Because the CCD camera is usually exposed for about *850-950 milliseconds*, several fans and a heat sink were attached for cooling purposes to effectively prevent image quality and resolution losses. A photodiode was also attached to the camera and the DAQ system to identify when the images were being taken by the camera in the same time domain as the thermocouple and pressure transducer readings (for future calibration purposes). Temporary voltage stagnations in photodiode readings identified image capture times. Stagnation temperature values were found by simply using ambient thermocouple readings. Stagnation and freestream static pressure data were obtained via pressure transducers in stagnation chamber and appropriate test-section location respectively.

TSP/PSP is a non-intrusive method to obtain flow diagnostics. A thin layer of paint is applied to a model surface, and then resulting fluorescence of the paint corresponds to a temperature or pressure. After proper calibration, the result is a 2D map of temperature/pressure with each pixel in the image acting as a measurement probe. This is much more efficient and less intrusive than using transducers or thermocouples on a surface when contours are desired. A disadvantage of this technique is that it does not provide time-resolved data.

In quantum mechanics, when photons are incident on matter, their energy can be absorbed if it corresponds to an allowable change in the internal structure of the molecule or atom. Depending on internal structure, the absorbed light is re-emitted at different frequencies – spectroscopic techniques such as TSP/PSP rely on this principle.

When in an excited state, there are two major mays for molecules to de-excite:
1) Photon emission: molecules de-excited by means of fluorescence.
2) Quenching: molecules de-excited by transferring rovibronic energy as a result of collisions with other molecules

With more quenching, less fluorescence; less quenching, more fluorescence. This tells us that as pressure/temperature increases, collisional/thermal quenching increases, which leads to an ultimate decrease in fluorescence. In other words, lower intensities relate to higher pressures/temperatures.

c) MTV/LDV/PIV

1. Molecular tagging Velocimetry
Non-reacting flwos must be seeded with an appropriate species when dealing with laser-induced fluorescence, such as Acetone, NO, Kr, etc. A pulsed laser is normally used to maintain high intensities over a larger timeframe.
In MTV, two images are acquired at a very small time separation (on the order of nanoseconds), and velocity can be obtained based on particle displacement.

2. Laser Doppler Velocimetry
Incoming flow is seeded with tracer particles (such as atomized oil droplets or TiO2 – must not alter flowfield by substantial amount) while overlapping laser beams focus a small interrogation volume. An optical detector measures intensity pattern at the overlap location – due to Doppler shifts in the scattered light as a result of particle motion, an interference pattern forms. This pattern can be related to velocity and allows for three components of velocity to be obtained at a single point.

3. Particle Image Velocimetry
Similar to LDV, the incoming flow is seeded with tracer particles. In this case, a laser sheet is pulsed twice with a known time-delay between pulses. The particle images are then captured on camera, and the velocity field is calculated from particle displacements. This method can be used to obtain two or three dimensional velocity fields.

d) Schematics for Experimental Tests

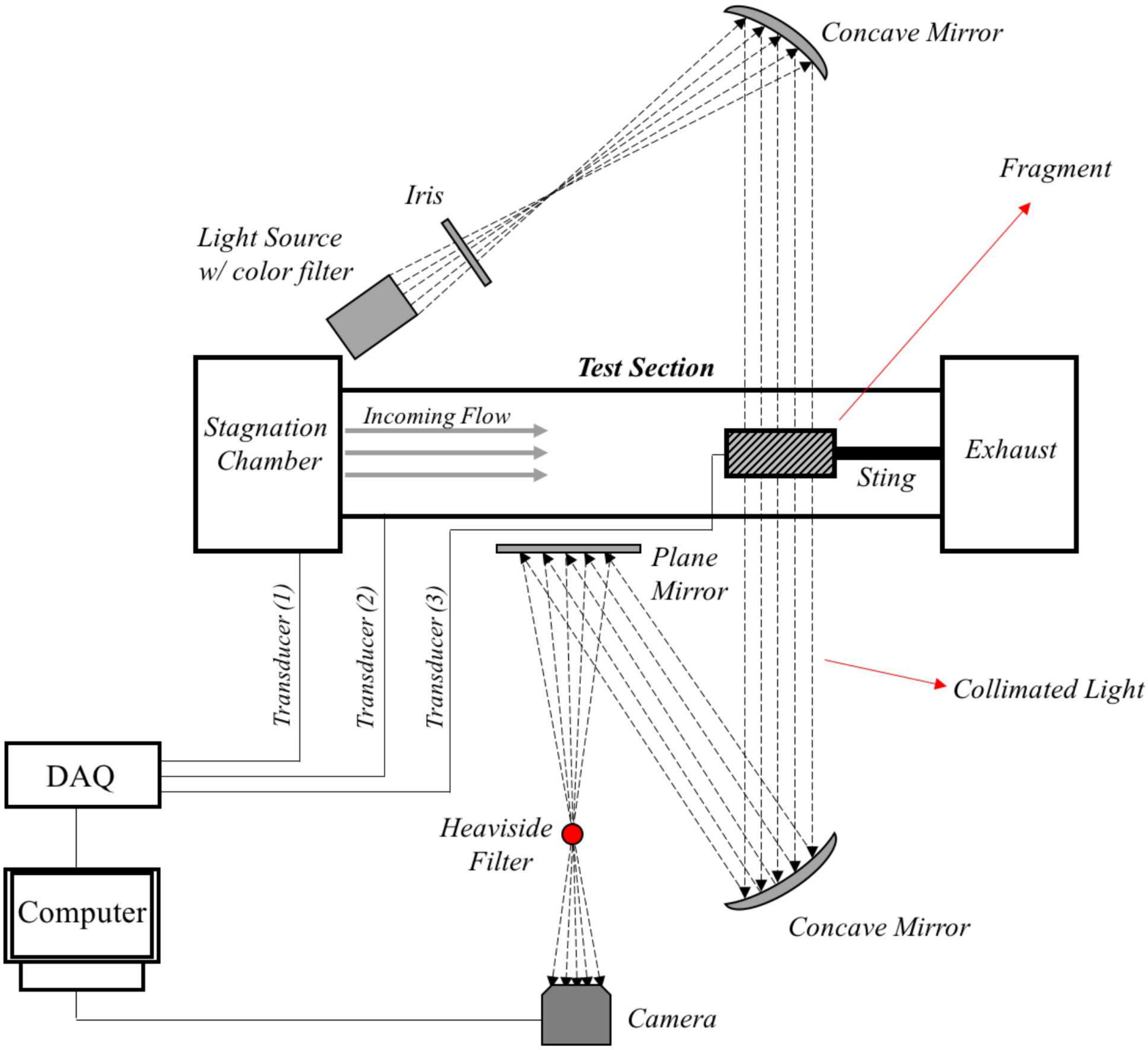

Figure 6. Schlieren experimental arrangement, top view.

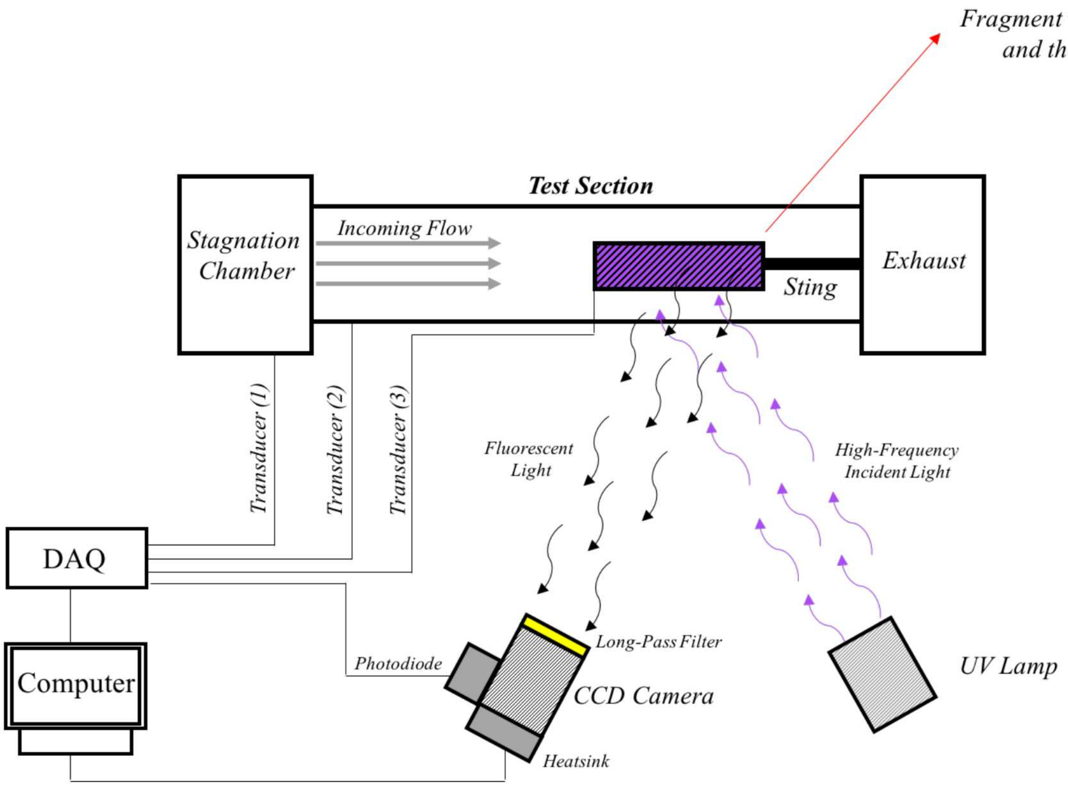

Figure 7. TSP experimental arrangement, top view.

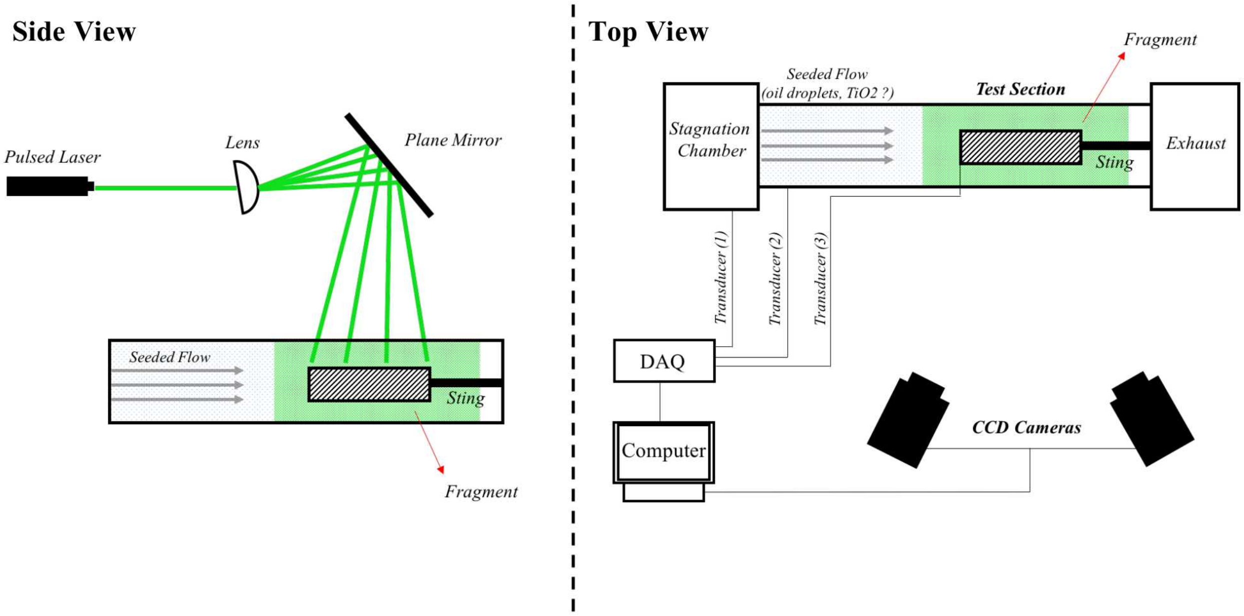

Figure 8. PIV experimental arrangement, side and top view.

e) Data Tables

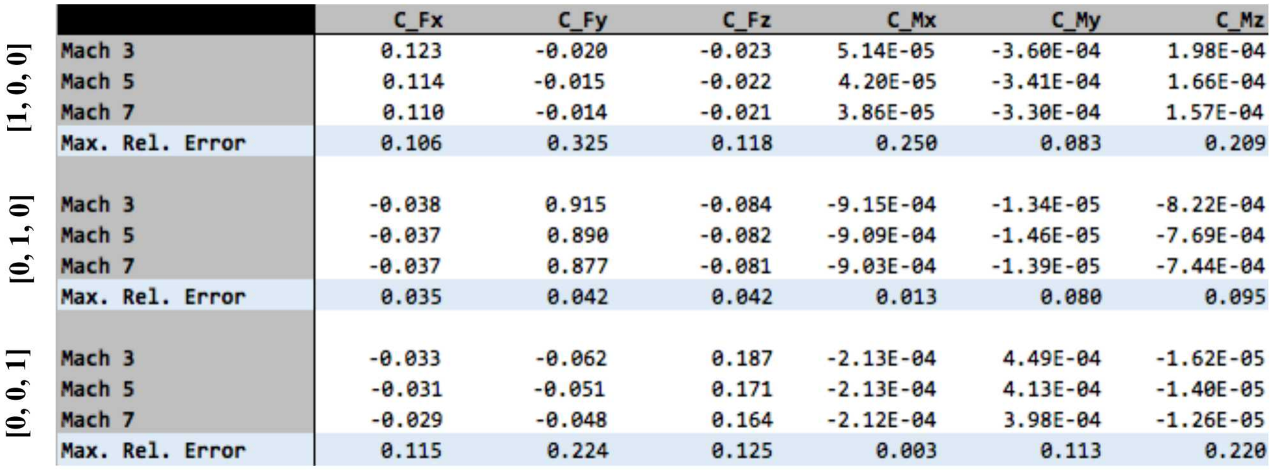

		C_Fx	C_Fy	C_Fz	C_Mx	C_My	C_Mz
[1, 0, 0]	Mach 3	0.123	-0.020	-0.023	5.14E-05	-3.60E-04	1.98E-04
	Mach 5	0.114	-0.015	-0.022	4.20E-05	-3.41E-04	1.66E-04
	Mach 7	0.110	-0.014	-0.021	3.86E-05	-3.30E-04	1.57E-04
	Max. Rel. Error	0.106	0.325	0.118	0.250	0.083	0.209
[0, 1, 0]	Mach 3	-0.038	0.915	-0.084	-9.15E-04	-1.34E-05	-8.22E-04
	Mach 5	-0.037	0.890	-0.082	-9.09E-04	-1.46E-05	-7.69E-04
	Mach 7	-0.037	0.877	-0.081	-9.03E-04	-1.39E-05	-7.44E-04
	Max. Rel. Error	0.035	0.042	0.042	0.013	0.080	0.095
[0, 0, 1]	Mach 3	-0.033	-0.062	0.187	-2.13E-04	4.49E-04	-1.62E-05
	Mach 5	-0.031	-0.051	0.171	-2.13E-04	4.13E-04	-1.40E-05
	Mach 7	-0.029	-0.048	0.164	-2.12E-04	3.98E-04	-1.26E-05
	Max. Rel. Error	0.115	0.224	0.125	0.003	0.113	0.220

Table 1. Force and moment coefficient data for fragment with relative errors w.r.t. orientation.

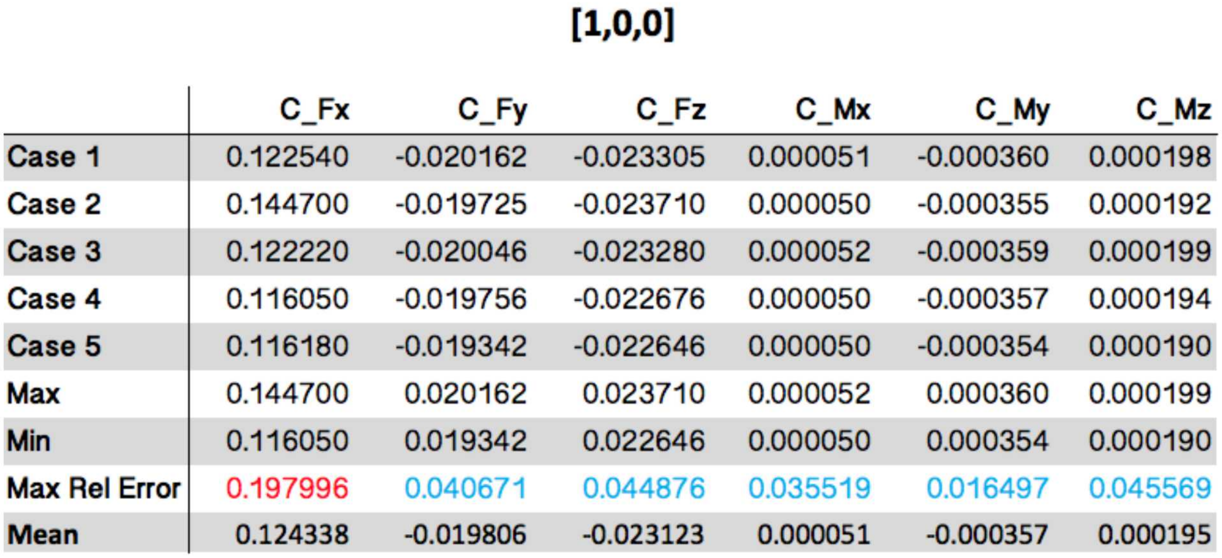

[1,0,0]

	C_Fx	C_Fy	C_Fz	C_Mx	C_My	C_Mz
Case 1	0.122540	-0.020162	-0.023305	0.000051	-0.000360	0.000198
Case 2	0.144700	-0.019725	-0.023710	0.000050	-0.000355	0.000192
Case 3	0.122220	-0.020046	-0.023280	0.000052	-0.000359	0.000199
Case 4	0.116050	-0.019756	-0.022676	0.000050	-0.000357	0.000194
Case 5	0.116180	-0.019342	-0.022646	0.000050	-0.000354	0.000190
Max	0.144700	0.020162	0.023710	0.000052	0.000360	0.000199
Min	0.116050	0.019342	0.022646	0.000050	0.000354	0.000190
Max Rel Error	0.197996	0.040671	0.044876	0.035519	0.016497	0.045569
Mean	0.124338	-0.019806	-0.023123	0.000051	-0.000357	0.000195

Table 2. Force and moment coefficient data for all five mesh cases in the [1,0,0] orientation.

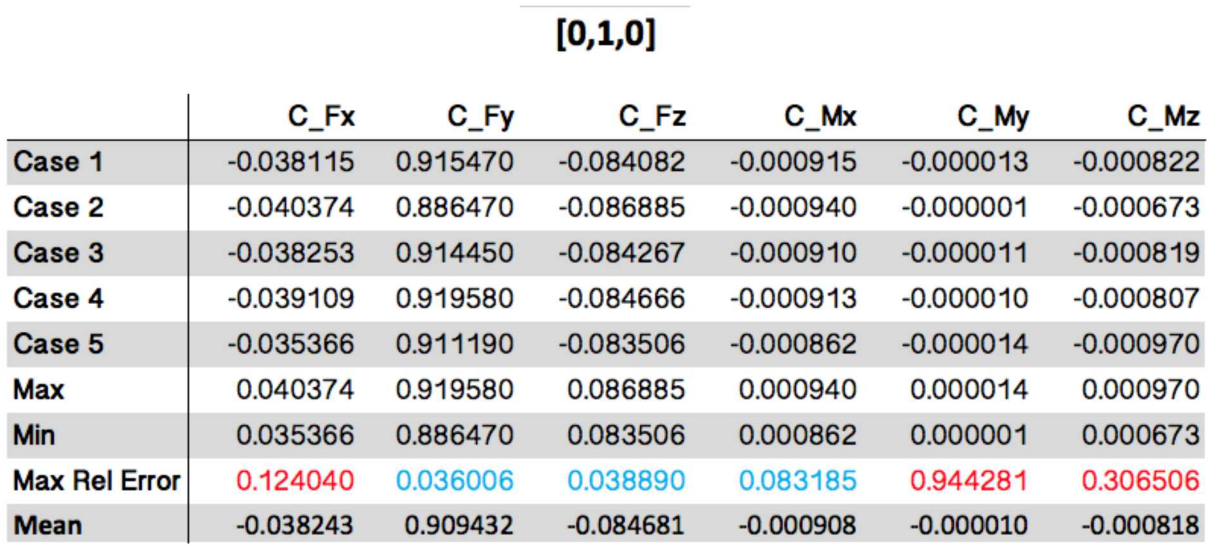

[0,1,0]

	C_Fx	C_Fy	C_Fz	C_Mx	C_My	C_Mz
Case 1	-0.038115	0.915470	-0.084082	-0.000915	-0.000013	-0.000822
Case 2	-0.040374	0.886470	-0.086885	-0.000940	-0.000001	-0.000673
Case 3	-0.038253	0.914450	-0.084267	-0.000910	-0.000011	-0.000819
Case 4	-0.039109	0.919580	-0.084666	-0.000913	-0.000010	-0.000807
Case 5	-0.035366	0.911190	-0.083506	-0.000862	-0.000014	-0.000970
Max	0.040374	0.919580	0.086885	0.000940	0.000014	0.000970
Min	0.035366	0.886470	0.083506	0.000862	0.000001	0.000673
Max Rel Error	0.124040	0.036006	0.038890	0.083185	0.944281	0.306506
Mean	-0.038243	0.909432	-0.084681	-0.000908	-0.000010	-0.000818

Table 3. Force and moment coefficient data for all five mesh cases in the [1,0,0] orientation.

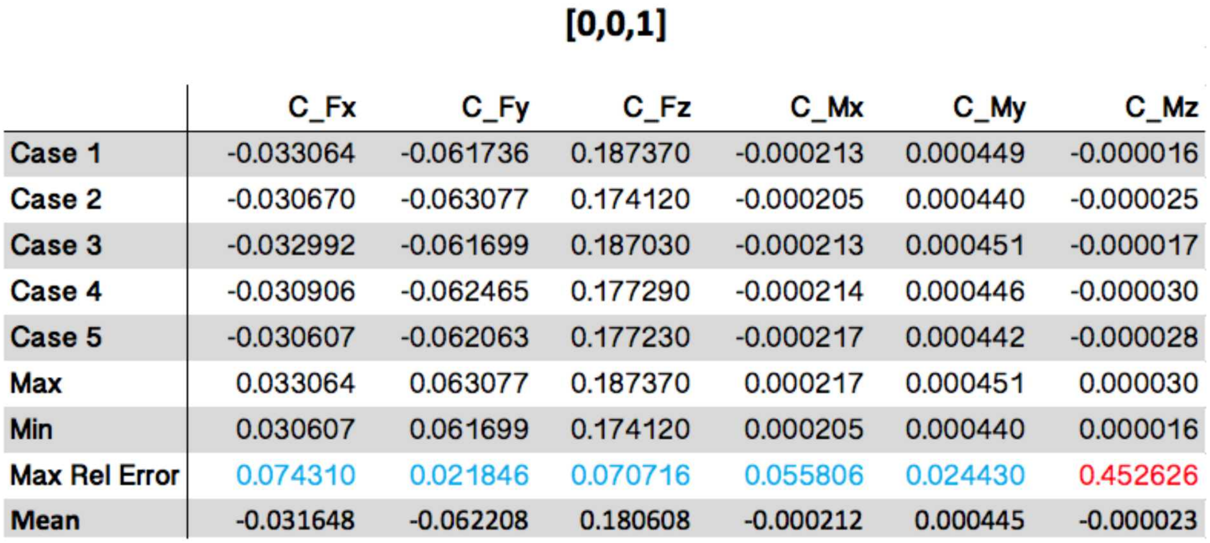

[0,0,1]

	C_Fx	C_Fy	C_Fz	C_Mx	C_My	C_Mz
Case 1	-0.033064	-0.061736	0.187370	-0.000213	0.000449	-0.000016
Case 2	-0.030670	-0.063077	0.174120	-0.000205	0.000440	-0.000025
Case 3	-0.032992	-0.061699	0.187030	-0.000213	0.000451	-0.000017
Case 4	-0.030906	-0.062465	0.177290	-0.000214	0.000446	-0.000030
Case 5	-0.030607	-0.062063	0.177230	-0.000217	0.000442	-0.000028
Max	0.033064	0.063077	0.187370	0.000217	0.000451	0.000030
Min	0.030607	0.061699	0.174120	0.000205	0.000440	0.000016
Max Rel Error	0.074310	0.021846	0.070716	0.055806	0.024430	0.452626
Mean	-0.031648	-0.062208	0.180608	-0.000212	0.000445	-0.000023

Table 4. Force and moment coefficient data for all five mesh cases in the [0,0,1] orientation.